The carbonation kinetics of calcium hydroxide nanoparticles: a Boundary Nucleation and Growth description

Accepted Manuscript

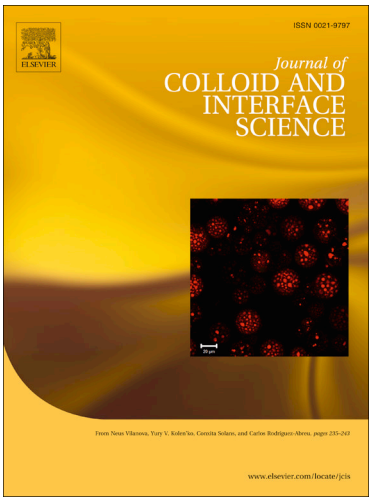

The carbonation kinetics of calcium hydroxide nanoparticles: a Boundary Nucleation and Growth description

R. Camerini, G. Poggi, D. Chelazzi, F. Ridi, R. Giorgi, P. Baglioni

PII: S0021-9797(19)30387-X
DOI: https://doi.org/10.1016/j.jcis.2019.03.089
Reference: YJCIS 24810

To appear in: *Journal of Colloid and Interface Science*

Received Date: 27 February 2019
Revised Date: 25 March 2019
Accepted Date: 26 March 2019

Please cite this article as: R. Camerini, G. Poggi, D. Chelazzi, F. Ridi, R. Giorgi, P. Baglioni, The carbonation kinetics of calcium hydroxide nanoparticles: a Boundary Nucleation and Growth description, *Journal of Colloid and Interface Science* (2019), doi: https://doi.org/10.1016/j.jcis.2019.03.089

The carbonation kinetics of calcium hydroxide nanoparticles: a Boundary Nucleation and Growth description

R. Camerini[a], G. Poggi[a], D. Chelazzi[a], F. Ridi[a], R. Giorgi[a], P. Baglioni[a*]

[a]Department of Chemistry "Ugo Schiff" and CSGI, University of Florence, Via della Lastruccia 3 – 50019 Sesto Fiorentino (FI), Italy

*Corresponding author: baglioni@csgi.unifi.it. Phone: +39 0554573033

Abstract

Hypothesis The reaction of $Ca(OH)_2$ with CO_2 to form $CaCO_3$ (carbonation process) is of high interest for construction materials, environmental applications and art preservation. Here, the "Boundary Nucleation and Growth" model (BNGM) was adopted for the first time to consider the effect of the surface area of $Ca(OH)_2$ nanoparticles on the carbonation kinetics.
Experiments The carbonation of commercial and laboratory-prepared particles' dispersions was monitored by Fourier Transform Infrared Spectroscopy, and the BNGM was used to analyze the data. The contributions of nucleation and growth of $CaCO_3$ were evaluated separately.
Findings During carbonation the boundary regions of the $Ca(OH)_2$ particles are densely populated with $CaCO_3$ nuclei, and transform early with subsequent thickening of slab-like regions centered on the original boundaries. A BNGM limiting case equation was thus used to fit the kinetics, where the transformation rate decreases exponentially with time. The carbonation rate constants, activation energies, and linear growth rate were calculated. Particles with larger size and lower surface area show a decrease of the rate at which the non-nucleated grains between the boundaries transform, and an increase of the ending time of $Ca(OH)_2$ transformation. The effect of temperature on the carbonation kinetics and on the $CaCO_3$ polymorphs formation was evaluated.

Keywords

Calcium hydroxide, calcium carbonate, nanoparticles, carbonation, kinetics, boundary nucleation and growth

Introduction

Nanostructured calcium hydroxide is a material of high interest, and has proven a competitive alternative to bulk hydroxides and other traditional compounds. Recent applications comprise the use of $Ca(OH)_2$ nanoparticles as flame-retardants for polymeric materials [1], antibacterial agents for medical purposes [2], and neutralizing agents for the deacidification of cellulose-based artworks [3–8].
Besides the direct use of calcium hydroxide nanoparticles, several fundamental applications involve the conversion of $Ca(OH)_2$ into calcium carbonate ($CaCO_3$) by reaction with atmospheric CO_2 in the presence of water, the so-called carbonation process. Examples include a secondary process in the hardening of Portland cement [9,10], the strengthening of construction materials [11–18], and environmental applications (carbon capture/storage, scrubber systems, geological disposal of waste) [19–23].

In particular, we pioneered the use of dispersions of $Ca(OH)_2$ nanoparticles in short-chain alcohols for the consolidation of carbonate-based immovable and movable works of art, which altogether represent the majority of the monumental and architectural patrimony of mankind [12,24,25].
The use of $Ca(OH)_2$ nanoparticles allows homogenous distribution of the particles inside matrices, good penetration in the porous material in need of consolidation, and faster conversion than micron-sized particles into crystalline calcium carbonate that produces mechanical strengthening [26,27]. These systems have been successfully employed to consolidate mortars, murals and stone, replacing traditional and detrimental adhesives such as synthetic polymers, which are known to alter the artifacts' surface [28–31] and must be removed with advanced cleaning tools (e.g. microemulsions and gels) [32–35] prior to the application of the particles.
Different synthetic processes have been developed over the last decades to tailor the $Ca(OH)_2$ particles' shape and size, crystallinity, and adsorbed additives [13,14,26,27,36–46], and an inclusive review of synthetic pathways has been recently provided by Navarro et al. [40]. However, while both the carbonation of bulk $Ca(OH)_2$ and the carbonation in solution have been addressed in the literature [47–51], our knowledge of the carbonation mechanism of nano-sized $Ca(OH)_2$ particles in air is still poor. The process is affected by several factors, including the particles' size, surface area, and impurities, as well as environmental parameters such as temperature, relative humidity (RH), and CO_2 concentration [52–54]. Different models have been proposed in the past years to fit the experimental data describing the transformation of calcium hydroxide into $CaCO_3$ phases. Some authors used deceleratory models with no induction time [50,51,54,55], while we found that a sigmoidal-type Avrami-Erofeev kinetic model provided a good fitting of the carbonation kinetics when the formation of the sole calcite phase (a better consolidant than metastable phases) is monitored [16]. Recently, Rodriguez-Navarro et al. highlighted that different results can be obtained by overlooking the role of precursor phases (e.g. amorphous calcium carbonate and vaterite) [52]; these authors monitored the formation of both amorphous and crystalline $CaCO_3$ phases through thermal analysis, and fitted the results to the solid-state deceleratory kinetic models summarized in a review by Khawam and Flanagan [56]. Among the different deceleratory models, the best fitting was obtained using a first order model [52].
In the present contribution, we investigated the carbonation kinetics of four different formulations of $Ca(OH)_2$ nanoparticles' dispersions, applying for the first time the mathematical "Boundary Nucleation and Growth" model (BNGM), originally developed by Cahn [57], and later used by Thomas to describe the hydration of tricalcium silicate (C_3S) grains [58]. The carbonation of $Ca(OH)_2$ nanoparticles is a water-mediated process that takes place at the solid-liquid interface [40,59–61]; therefore, the BNGM was here evaluated considering that the process is expected to preferentially occur via nucleation at the grain boundaries, followed by growth along the particles surface, and then outward into the pore space between the particles, until the products regions coalesce. Namely, this geometrical model takes into account the effect of the surface area of the particles on the carbonation kinetics.
After selecting the BNGM based on the aforementioned rationale, we followed a rigorous approach by evaluating separately the contributions of the nucleation and growth of $CaCO_3$ during the carbonation process. Thus, we evaluated the possible application of limiting cases of the model, where one of the two contributions (i.e. either boundary nucleation or growth) prevails over the other.
Fourier Transform Infrared Spectroscopy (FTIR) was selected to investigate the carbonation process, as it feasibly allows monitoring over time the transformation of calcium hydroxide into both amorphous and crystalline calcium carbonate phases [62,63]. In this contribution, the main focus was the quantitative description of the calcium hydroxide reaction kinetics, using a mathematical model able to describe processes at the interface of the reacting grains. To this purpose, the consumption of calcium hydroxide over time was monitored by FTIR, fitting the experimental data to the BNGM, and matching the obtained results with the characteristics of the hydroxide nanoparticles (size, surface area, dispersing solvent). The hydroxide consumption was

followed under strictly controlled environmental conditions (T, RH, CO_2 concentration), evaluating the effect of temperature on the process.
Finally, as a side topic to the actual kinetic study, we carried out a semi-quantitative evaluation of the formed stable (calcite) and metastable (vaterite, aragonite) crystalline $CaCO_3$ phases for the different systems. Rather than a morphological and structural study of the $CaCO_3$ polymorphs, our aim was to verify if the size and surface area of the $Ca(OH)_2$ nanoparticles affect the speed of formation of vaterite and calcite. FTIR was used to evaluate the presence of $CaCO_3$ phases, as this technique was previously reported in the literature to quantitatively analyze calcium carbonate polymorphs [63].
We prepared two of the systems investigated in this study following two different synthetic routes for the preparation of $Ca(OH)_2$ nanoparticles' dispersions, i.e. the treatment of slaked lime and a solvothermal process. Namely, slaked lime can be treated through a top-down process, and the obtained particles are stably dispersed in short-chain alcohols [13,24]. In solvothermal processes, the alcohol (ethanol or propanol) oxidizes metallic calcium to the corresponding alkoxide, and the subsequent addition of water induces the formation of calcium hydroxide via a hydrolysis reaction [64,65]. As a reference, a commercial formulation (CaLoSiL®) was also investigated; the dispersions (either in ethanol or 2-propanol) are prepared via an alkoxide route [11,40].
The four systems exhibit different characteristics, such as the used liquid medium (ethanol, 2-propanol), and the specific surface area of the particles. The kinetic behavior of the four systems was thus compared, calculating the rate constants, the activation energies, and the linear growth rate of the carbonation process.

Materials and Methods

Chemicals

KBr (FTIR grade, Merck), NaCl (Technical grade, Sigma-Aldrich) were used as received. Ethanol absolute (99.8%, Fluka), 2-propanol (99.5%, Sigma-Aldrich), slaked lime ($Ca(OH)_2$, technical grade, Banca della Calce) and metal granular calcium (99%, Aldrich) were used for the syntheses of nanoparticles. Water was purified by a Millipore Milli-Q UV system (resistivity >18 MΩ cm).

Dispersions of nanoparticles

A dispersion (5 g/L) of $Ca(OH)_2$ nanoparticles was prepared by treatment (grinding and sonication) of slaked lime [13,24], and labeled as LIP (Laboratory-prepared formulation, particles dispersed in 2-propanol). An IKA Ultraturrax dispersing system and a Branson Ultrasonics Sonifier S-450 were used. Following a solvothermal route reported elsewhere [64,65], we prepared a concentrated (35 g/L) dispersion in ethanol, which was then diluted to 5 g/L, and labeled as LE. The synthesis was performed in a high-pressure reactor (Parr-instruments).
The commercial products CaLoSiL®E5 and CaLoSiL®IP5 are $Ca(OH)_2$ nanoparticles alcohol dispersions (5 g/L) commercialized by IBZ-Salzchemie GmbH & Co. KG (Germany). The systems have been labeled as CE and CIP (particles commercially produced, dispersed respectively in ethanol (CE) and 2-propanol (CIP)). In Table 1, the name, composition, and some physico-chemical parameters of the nanoparticles dispersions, are reported.

Table 1 – Name, composition, size, specific surface area and total area of the grain boundaries per unit volume (O_V^B) of the $Ca(OH)_2$ nanoparticles dispersions selected for the carbonation kinetics.

SYSTEM NAME	SOLVENT	PREPARATION	PART. SIZE (nm)	SPEC. SURF. AREA ($m^2 \cdot g^{-1}$)	O_V^B (μm^{-1})
CE	ethanol	Solvothermal process from Ca	50-250	38	76
LE	ethanol		100-200	36	72
CIP	2-propanol		50-250	38	76
LIP	2-propanol	Top-down process from slaked lime	300-500 (with few micron-sized aggregates)	20	40

The particles' size for the commercial systems (CE, CIP) are extracted from their Technical Leaflet [66]. The particles' size distribution of the LE and LIP systems was measured through Dynamic Light Scattering (DLS) measurements, which were performed with a 90Plus Particle Size Analyzer (Brookhaven Instrument Corporation). The light scattered from the sample was collected at 90˚ with the incident 659 nm laser light radiation. At least three measurements for each sample were recorded, at 25˚C. Particle size distributions were obtained from the fitting of the measured autocorrelation functions using the CONTIN method [67]. Each sample was diluted to 1 g/L before the measurement.
The specific surface area of nanoparticles (see Table 1) was determined by Brunauer-Emmett-Teller (BET) measurements (at least two measurements for each sample). N_2 sorption isotherms were obtained using a Coulter SA 3100 Surface area analyzer. This gives access to the value of the surface area with an error of about 5%.

Carbonation of nanoparticles and FTIR analysis

The carbonation of $Ca(OH)_2$ nanoparticles occurred under controlled environmental conditions, in a home-made sealed climatic chamber. Temperature and RH were continuously monitored using a data logger (Easylog EL-USB-2-LCD, 1 reading every 5 minutes). RH was kept stable at 75 (± 2) % placing NaCl saturated solutions inside the chamber. The carbonation took place at temperature values set at 14, 22 and 30 (± 1.5) °C. Similar temperature and RH values have been used in previous aging protocols where the nucleation of calcium carbonate from $Ca(OH)_2$ particles was studied [52,68,69]. These values were selected since they are representative of standard conditions typically found in case studies where the particles' dispersions are applied (e.g. consolidation of stone and mortars). Environmental CO_2 concentration in the chamber was 450 ppm (monitored with an AirControl 3000 CO_2, Dostmann Electronics), consistent with previous studies on the carbonation of $Ca(OH)_2$ [59,70]. A fan was used to prevent carbon dioxide deposition on the bottom of the climatic chamber.

For the FTIR study of the carbonation process, thin films of calcium hydroxide were cast on KBr pellets. Each pellet was prepared using 200 mg of KBr. KBr was dried overnight in an oven under vacuum at 110˚C, prior to pellet preparation. For each measurement, before deposition of $Ca(OH)_2$, the pellet was placed on a holder, and used to acquire a background FTIR spectrum. Then, 40 μL of nanoparticles' dispersion was deposited over the pellet, still placed on the holder, and dried under N_2 flow to ensure complete solvent evaporation without triggering the carbonation reaction. A spectrum was acquired on the pellet, and the holder was then placed into a climatic chamber. At chosen time, the pellet was extracted from the chamber and another spectrum was acquired. As the extraction of the pellet and its short permanence in laboratory conditions (23°C, 50% RH) alter the carbonation process, each pellet was discarded after the measurement, i.e. different pellets were used for different carbonation times. At least three pellets were prepared and measured for each carbonation time. The FTIR spectra were acquired using a BIO-RAD FTS-40 spectrometer, in transmission mode, between 4000 and 400 cm^{-1}, acquiring 64 scans for each spectrum, and using a delay time of 30 s between placing the KBr pellet in the sample holder and acquiring the spectrum. The Win-Ir software was used to calculate the area of the absorption peak of $Ca(OH)_2$ centered at 3650 cm^{-1} (OH stretching [71]), using a linear baseline. The evolution over time of this peak, during the carbonation process, was calculated as follows:

$$\alpha = \frac{(Area_{t0} - Area_{tx})}{Area_{t0}}$$

where $Area_{t0}$ is the area of the peak at $t = 0$, and $Area_{tx}$ is the area of the peak at generic time $t = x$, measured for the same KBr pellet and on the same spot. Thus, α is defined as the carbonation degree, increasing from 0 to 1 upon completion of the carbonation process.

Generalized Boundary Nucleation and Growth Model (BNGM)

Because the carbonation of $Ca(OH)_2$ nanoparticles is a process occurring at the interface of the particles, it can not be assumed that the nucleation of calcium carbonate takes place at randomly distributed locations within the untransformed $Ca(OH)_2$ volume. Instead, the carbonation products form first on the surface of the particles (grain boundary nucleation), and then grow along the particles' surface, eventually covering them. Product regions from adjacent particles eventually coalesce.

The kinetics of nucleation and growth under the conditions of grain boundary nucleation were derived mathematically by Cahn [57], discussed and implemented by Christian [72], and later used by Thomas to describe the hydration of tricalcium silicate (C_3S) grains [58]. These works can be referred to for the detailed geometrical derivation of the BNG kinetic model.

Essentially, the derivation of the model's equations starts by considering an untransformed volume containing single planar boundary, and assuming that nucleation of the transformed phase occurs only at spatially random locations on this boundary. Then, the intersection of a single growing spherical region of nucleated product with a plane parallel to the boundary (at a perpendicular distance *y*) is considered. The volume fraction of transformed phase originating from nuclei on the single grain boundary is thus found by integrating the area fraction of intersection over all values of the perpendicular distance *y* between the plane and the boundary.

According to the generalized BNGM, the volume fraction of transformed phase originating from nuclei on the same grain boundary, *X*, can be expressed as follows [58]:

$$X = 1 - exp\left[-2O_V^B \int_0^{Gt}(1 - exp(-Y^e))dy\right] \qquad \text{Eq. 1}$$

where O_V^B is the total area of the grain boundaries (randomly distributed in the original untransformed volume) per unit volume, G is the linear growth rate, t is the time since the start of the transformation; y is the perpendicular distance of a plane parallel to the boundary from the transforming boundary (i.e., Gt), Y^e is the extended area fraction of the intersection between the plane at distance y from the boundary and all regions nucleated on the grain boundary. Y^e can be mathematically described as:

$$Y^e = \frac{\pi I_B}{3} G^2 t^3 \left[1 - \frac{3y^2}{G^2 t^2} + \frac{2y^3}{G^3 t^3}\right] \qquad if \;\; t > y/G \qquad \text{Eq. 2}$$

$$Y^e = 0 \qquad if \;\; t < y/G$$

where I_B is the nucleation rate per unit area of untransformed boundary.
The volume of the transformed phase, X, depends thus on G, I_B, and O_V^B; however, these parameters are covariant, such that Eq. 1 has only two degrees of freedom. For this reason, Thomas proposed to describe the kinetics in terms of two independent rate constants, named k_B and k_G, which are defined respectively as the rate at which the nucleated boundary area transforms, and the rate at which the non-nucleated grains between the boundaries transform (i.e. the rate at which the porosities are filled with reaction products) [58,73]. The linear growth rate, G, and the nucleation rate I_B, are obtained from the rate constants k_B and k_G, by the following relationships:

$$k_B = (I_B O_V^B)^{1/4} G^{3/4} \qquad \text{Eq. 3}$$

$$k_G = O_V^B G \qquad \text{Eq. 4}$$

To achieve a numerically solvable equation, a change of variable from $y = Gt$ to $z = y/G$ is performed [58]:

$$Y^e = \frac{\pi}{3} \frac{{k_B}^4}{k_G} t^3 \left[1 - \frac{3z^2}{t^2} + \frac{2z^3}{t^3}\right] \qquad if \;\; t > z \qquad \text{Eq. 5}$$

and hence:

$$X = 1 - exp\,[-2k_G \textstyle\int_0^t (1 - exp(-Y^e))dz] \qquad \text{Eq. 6}$$

Eq. 6 can now be computed numerically, and the parameters k_B and k_G can be directly accessed by the fitting procedure implemented in the analysis software. Monitoring the disappearance of calcium hydroxide gives direct access to the progress of the carbonation. The reaction degree α versus time can be directly fitted using the generalized BNGM by explicitly introducing α into Eq. 6:

$$\alpha_t = \alpha_i + \alpha_f \{1 - ex\,p[-2k_G \textstyle\int_0^t (1 - exp(-Y^e))dz]\} \qquad \text{Eq. 7}$$

where α_t is the fraction of converted calcium hydroxide at time t, and α_i and α_f are the fractions at initial and final time, respectively. Fitting the time evolution of α using Eq. 7 and Eq. 5 returns the two independent parameters k_B and k_G. The values of the linear growth rate, G, and of the nucleation rate, I_B, can be then calculated through Eq. 3, using k_B, k_G, and O_V^B. The values of O_V^B for the systems CE, LE, CIP, and LIP, are reported in Table 1. O_V^B was obtained dividing the surface area of the dry $Ca(OH)_2$ powder (see Table 1) by the volume occupied by the carbonation products after complete carbonation (per gram of reacting hydroxide, 0.5 cm^3/g). Such a volume was calculated from the stoichiometry of the reaction (see Eq. 8), using the density of the stable $CaCO_3$ polymorph,

calcite, i.e. 2.71 g/cm^3 (which is close to the average of the densities of the three crystalline polymorphs). The BNGM equations have been solved in Igor Pro, version 6.2.

Results and Discussion

Kinetic study

The carbonation of $Ca(OH)_2$ in humid conditions can be outlined in two main steps: the dissolution of the reactants, and the reaction of the ions in the presence of water. Namely, CO_2 diffuses at the gas/water interface and dissolves in water, forming carbonic acid (H_2CO_3), which dissociates into carbonate ions (CO_3^{2-}) and bicarbonate ions (HCO_3^-); $Ca(OH)_2$ dissolves and dissociates into calcium ions (Ca^{2+}) and hydroxyl ions (OH^-); the calcium ions and carbonate ions react leading to the precipitation of solid calcium carbonate ($CaCO_3$) [40,59–61]. The overall process is usually schematized as follows [Eq. 8]:

$$Ca(OH)_2 + CO_2 \leftrightarrow CaCO_3 + H_2O \qquad \text{Eq. 8}$$

According to Rodriguez-Navarro et al., the process follows the Ostwald's step rule, where amorphous calcium carbonate (ACC) is firstly formed, followed by metastable phases, before calcite forms (vaterite → aragonite → calcite) [52]. The formation of ACC pseudomorphs after $Ca(OH)_2$ involves multilayer adsorption of water onto the hydroxide crystals, followed by a dissolution-precipitation mechanism [52,53]. Both capillary condensation into the mesoporous structure, formed upon drying of the $Ca(OH)_2$ nanoparticles' dispersions, and the release of water during carbonation, favor the formation of ACC in the aqueous solution film (where high supersaturation is reached during the early stages) [51,52]. In addition, these authors observed ACC nanoparticles with no spatial connection with the ACC pseudomorphs; thus, they suggested that the particles might form through homogeneous nucleation in the aqueous solution film [52].

In order to select a kinetic model to describe the transformation of calcium hydroxide into carbonate, we considered that the formation of ACC in the aqueous film reasonably occurs along the surface of the $Ca(OH)_2$ nanoparticles (at the solid-liquid interface); the products eventually cover the surface and fill the mesoporous structure formed by the particles' aggregation after alcohol evaporation. Overall, the process can be considered analogous to a phase transformation in a polycrystalline solid where nucleation occurs preferentially at the grain (particle) boundaries. Therefore, the generalized BNGM [57,72] was adopted to describe the kinetics process. Previously, Thomas successfully applied this model to the hydration kinetics of tricalcium silicate (C_3S), i.e. another process that involves dissolution-precipitation and the formation of products on the surface of the C_3S particles via boundary nucleation and growth [58,74,75]. Following this rationale, in the present study we adopted a rigorous approach where we first verified the applicability of the generalized BNGM to describe the carbonation of the $Ca(OH)_2$ nanoparticles' dispersions. This enabled the evaluation of the single processes relevance (nucleation, growth) on the overall kinetics; thus, we were eventually able to provide the best fit of the curves taking advantage of a "limiting case" of the BNG model.

Figure 1 shows the time evolution of the carbonation degree (as obtained by FTIR) for the CE system at 22˚C. The remaining carbonation curves for all the systems (CE, LE, CIP, LIP) at the three considered temperatures (14, 22, and 30˚C) are shown in the SI (Figures S1-S4).

In Figure 1A, the carbonation curve was fitted to the generalized BNGM. The fitting directly yields the two rate constants k_B and k_G, i.e. the rate at which the nucleated boundary area transforms, and the rate at which the porosities are filled with carbonation products [58,73]. Table 2 summarizes the values of k_B and k_G for CE, LE, CIP and LIP, at the three temperatures.

Table 2 – Rate constants (k_B and k_G) of the four systems at the three temperatures, directly obtained by fitting the experimental data to the generalized BNGM.

SYSTEM NAME	14ºC		22ºC		30ºC	
	k_B (h^{-1})	k_G (h^{-1})	k_B (h^{-1})	k_G (h^{-1})	k_B (h^{-1})	k_G (h^{-1})
CE	0.66 ± 0.07	0.27 ± 0.03	1.58* ± 0.14	0.73 ± 0.11	2.75 ± 0.45	0.74 ± 0.07
LE	0.96* ± 0.19	0.28 ± 0.03	1.40* ± 0.16	0.50 ± 0.04	1.46 ± 0.13	0.60 ± 0.07
CIP	0.90* ± 0.16	0.22 ± 0.03	1.66 ± 0.55	0.32 ± 0.03	2.10* ± 0.20	0.84 ± 0.09
LIP	0.74* ± 0.26	0.12 ± 0.01	1.05 ± 0.48	0.13 ± 0.01	1.55 ± 0.26	0.35 ± 0.03

*These values could be obtained only by constraining the k_B value to the minimum necessary to make the fitting converge.

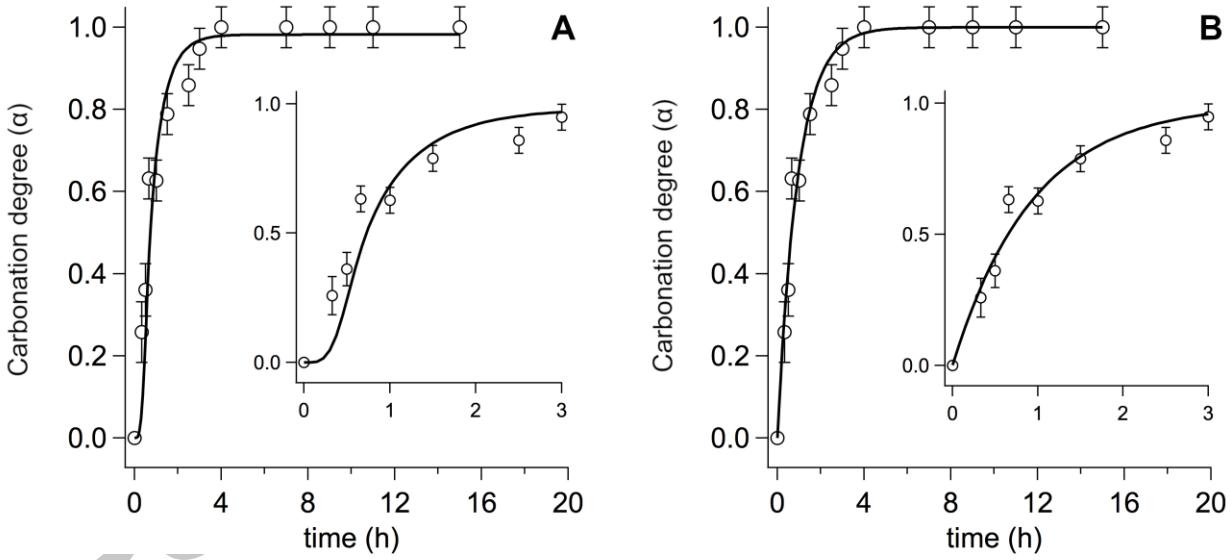

Figure 1 – Fitting of the carbonation curve of the CE system at 22°C, using (A) the generalized BNGM and (B) the limiting case BNGM. The insets highlight the different shape of the curves at the beginning of the kinetics (first 3 hours).

It is worth noting that in many cases the fitting does not converge unless the k_B value is constrained (values highlighted with a "*" in Table 2). In such cases we chose to constrain the k_B value to the minimum necessary to make the fitting converge, and the obtained values can be considered as the lowest possible estimations of k_B. Nevertheless, k_B is always higher than k_G, indicating that nucleation proceeds at a faster pace with respect to growth.

The linear growth rate, G, and the nucleation rate, I_B, can be calculated from k_B and k_G, using Eq. 3 and 4. The obtained I_B/G ratios are significantly large for all the considered systems and temperatures (*e.g.* ratios ranging from 10^4 to 10^7 $\mu m^{-1}h^{-2}$). According to Thomas, this indicates that the boundary regions are densely populated with nuclei and transform completely early in the process [58]. This means that the transformation does not depend on the nucleation rate, and occurs

mostly by subsequent thickening of slab-like regions of transformed product centered on the original boundaries [58]. Under these conditions, a limiting case equation (Eq. 9) is used to describe the process kinetics, where the transformation rate decreases exponentially with time [57]:

$$X = 1 - \exp[-2k_G t] \quad \text{Eq. 9}$$

Therefore, we proceeded to fit the carbonation curves with Eq. 9. Figure 1 shows the comparison between the generalized BNGM and the BNGM limiting case applied to the CE system at 22°C. Indeed, the use of the BNGM limiting case allows for a good fitting of the data without using narrow constraints, differently from the application of the generalized model. As clearly shown in Figure 1B, the fitting curve is exponential (independent on k_B), rather than sigmoidal (Figure 1A). The demonstration provided here, i.e. that the kinetics is independent on the nucleation rate, corroborates and integrates the findings of other authors that employed either first order [52] or pseudo-second order [50,51] deceleratory models to describe the carbonation kinetics of $Ca(OH)_2$ particles of different size (nano an sub-micro), in different environmental conditions. It must be noticed that none of these previous models addressed specifically the role of boundary nucleation and growth; *namely, no values for the growth constant rate were provided in those works.*
Fitting the curves under the BNGM limiting case directly yields the k_G values, which are reported in Table 3. The table also includes the G values (calculated from Eq. 4), and the ending time (t_f) of the $Ca(OH)_2$ transformation, i.e. when the absorption peak of $Ca(OH)_2$ centered at 3650 cm^{-1} (OH stretching) is no longer observable in the FTIR spectra of the nanoparticles' films.

Table 3 – Parameters extracted from the limiting case BNGM fitting of the CE, LE, CIP, and LIP systems at the three considered temperatures (ending time (t_f) of the $Ca(OH)_2$ transformation, rate constant (k_G [h^{-1}]), and calculated linear growth rate (G [$nm \cdot h^{-1}$])), and from the Arrhenius plots for the four systems (activation energy, E_a [$kJ \cdot mol^{-1}$], and R^2).

SYSTEM NAME	14°C			22°C			30°C			E_a	R^2
	t_f	k_G	G	t_f	k_G	G	t_f	k_G	G		
CE	5	0.23 ± 0.01	3.03 ± 0.28	4	0.53 ± 0.04	6.97 ± 0.88	3	0.67 ± 0.03	8.82 ± 0.84	50.4	0.90
LE	5	0.25 ± 0.01	3.47 ± 0.31	3	0.43 ± 0.02	5.97 ± 0.58	3	0.50 ± 0.03	6.94 ± 0.76	31.4	0.91
CIP	5	0.19 ± 0.01	2.50 ± 0.26	4	0.32 ± 0.02	4.21 ± 0.47	2.5	0.71 ± 0.03	9.34 ± 0.86	59.6	0.98
LIP	9	0.12 ± 0.01	3.00 ± 0.40	8	0.14 ± 0.01	3.50 ± 0.43	6	0.32 ± 0.01	8.00 ± 0.65	43.9	0.86

As expected, for each system the conversion of $Ca(OH)_2$ nanoparticles into $CaCO_3$ is faster (i.e. higher k_G values) at higher temperatures. A representative example is shown in Figure 2, where the fitted carbonation curves of LIP display a higher slope passing from 14 to 22 and 30˚C (Figure 2A-C). Fitted carbonation curves, using the BNGM limiting case, of the CE, LE and CIP systems are reported in Figure S5-S7. Besides, increasing the temperature, the curves reach the asymptotic plateau at earlier time. At all temperatures, LIP exhibits k_G values lower than the other systems, and roughly double t_f values (see Table 3 and Figure 3). This was explained considering that the

$Ca(OH)_2$ nanoparticles in LIP have larger dimensions (a bimodal distribution, with primary particles of 300-500 nm and larger aggregates of about 1 μm) and lower surface area than the other systems, as reported in Table 1; this results in a lower amount of boundaries available for the nucleation of $CaCO_3$, hence in a reduced reactivity during the carbonation process. At each temperature, the CE, LE and CIP systems exhibit roughly the same t_f values, and the values of k_G of these systems are more similar to each other than to the k_G value of LIP. This highlights that the kinetic behavior is influenced by the preparation method of the particles' dispersions, as it determines the particles' size and surface area, which are comparable for the systems CE, LE and CIP (see Table 1).

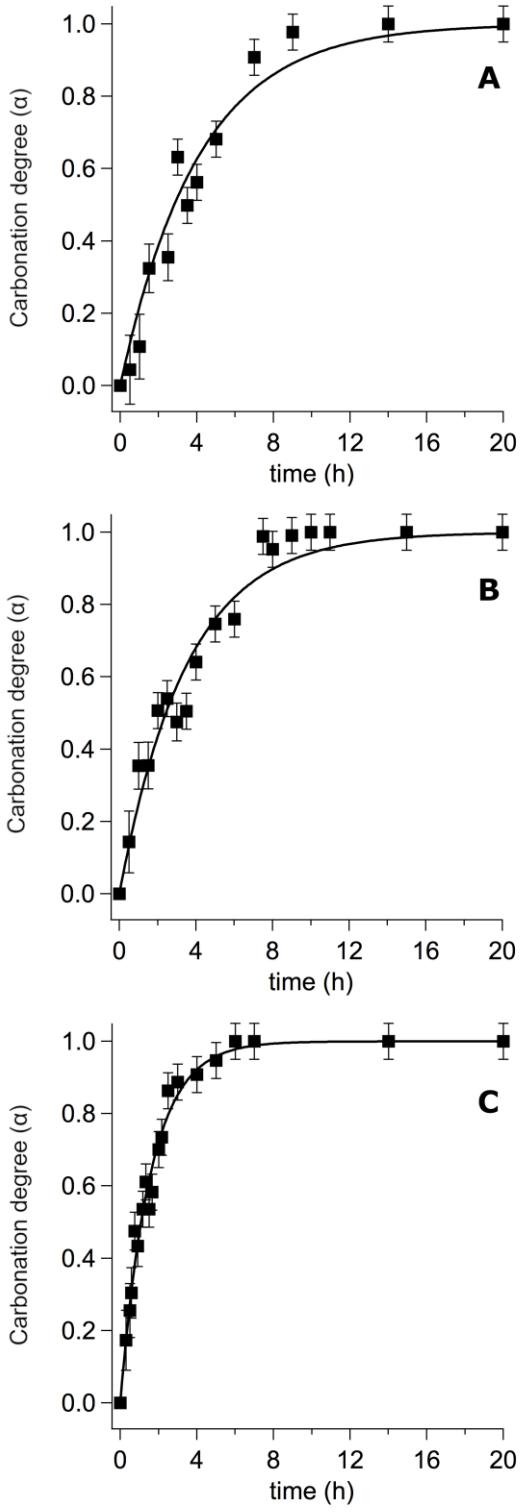

Figure 2 – Fitting of the carbonation curves of LIP at (A) 14°C, (B) 22°C, (C) 30°C, using the limiting case BNGM.

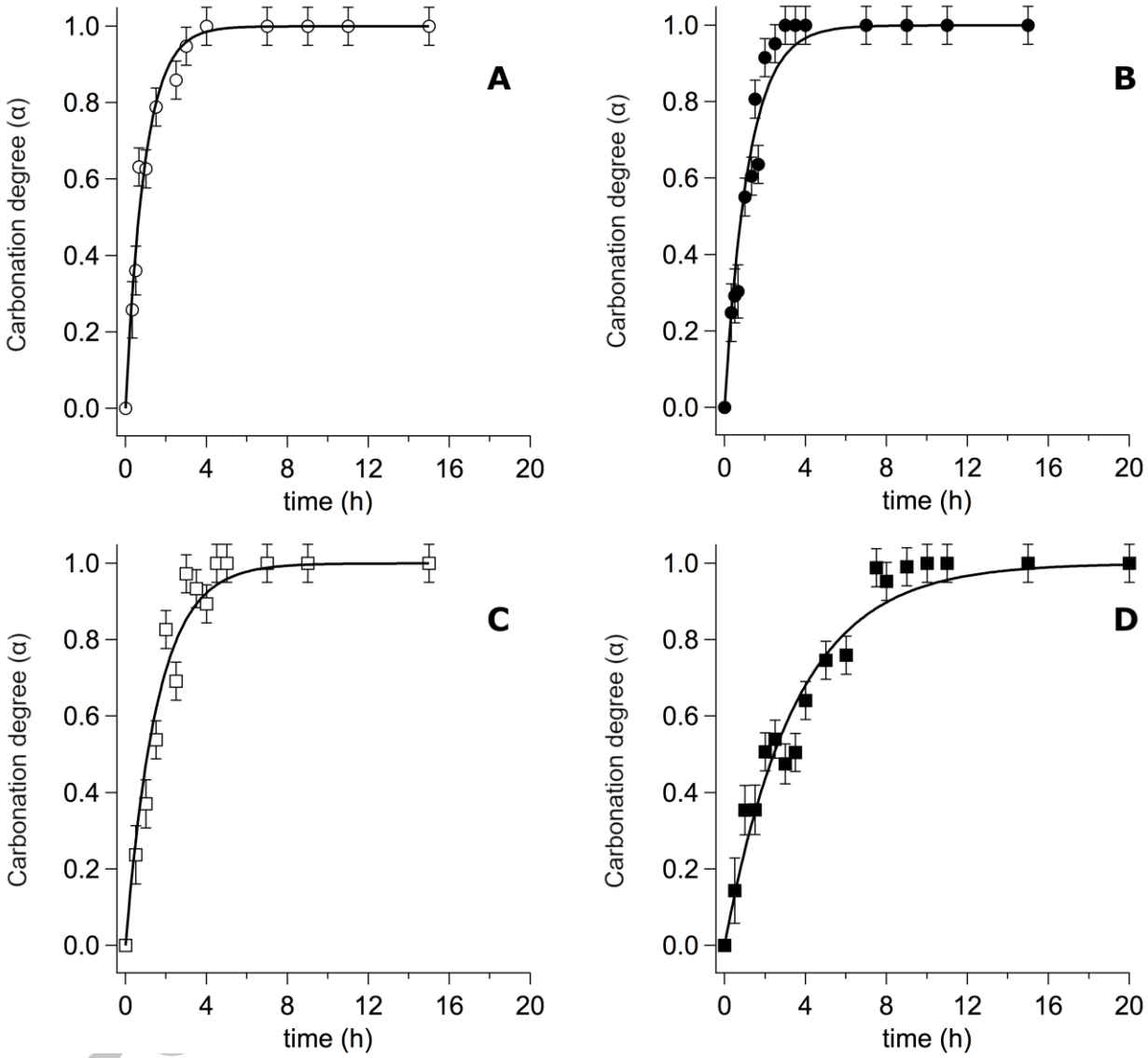

Figure 3 – Fitting of the carbonation curves at 22°C for (A) CE, (B) LE, (C) CIP, (D) LIP, using the limiting case BNGM.

The linear growth rate (G) has comparable values for the four systems at 14˚C (G ~3 nm·h^{-1}) and 30˚C (G ~8 nm·h^{-1}), while at 22˚C the systems in ethanol have a G value that is 1.5-2 times higher than systems in 2-propanol (G ~6-7 nm·h^{-1} for CE, LE; G ~4 nm·h^{-1} for CIP, LIP). The differences in G, observable at the intermediate temperature (22˚C), could be due to the role of the solvent in the formation of aggregates in the $Ca(OH)_2$ films. In fact, after the deposition of the nanoparticles' dispersions on the KBr pellets, alcohol evaporation leads to the formation of layers of stacked and aggregated particles. 2-propanol has a lower dielectric constant than ethanol, which results in lower Debye lengths and reduced screening between the particles in dispersion. This trend might translate into differential aggregation of the particles during alcohol evaporation and in the dry films, with more pronounced aggregation (and lower G values) in the case of particles in 2-propanol. We thus hypothesized that the aggregation state of the particles has a different influence on the surface area

of the dry $Ca(OH)_2$ films (which is similar for CE, LE, and CIP), and on k_G (which varies among the systems), i.e. the two factors that determine *G*. Instead, at 14˚C and 30˚C, the transformation of calcium hydroxide is respectively too slow or too fast in all systems to observe a significant difference in the linear growth rate of the transformation products; *in other terms, in these conditions the influence of T on G is more significant than that of the solvent*.

The activation energy of the $Ca(OH)_2$ transformation was calculated from Arrhenius plots (ln k_G versus 1/T) for the four systems, reported in Figure 4. Good R^2 values (0.86-0.98, see Table 3) were obtained from the linear fitting of the experimental data, indicating that the plots are linear across the considered temperature range. The slope of the linear fittings gives constant activation energies (E_a), which are reported in Table 3. Namely, it was found that the LE system exhibits the lowest dependence of k_G from temperature (E_a = 31.4 kJ·mol^{-1}), LIP has E_a = 43.9 kJ·mol^{-1}, and the two CaLoSiL® products show different activation energies (E_a = 50.4 kJ·mol^{-1} for CE, and 59.6 kJ·mol^{-1} for CIP), possibly due to the different solvents used. To the best of our knowledge, this is the first time that activation energy values are provided for the carbonation of $Ca(OH)_2$ nanoparticles around room temperature and environmental CO_2 concentration.

Elsewhere, activation energy values of 6-12 kJ·mol^{-1} have been reported for the dry solid-gas carbonation of micrometric aggregates of $Ca(OH)_2$ nano-platelets or micron-sized particles at high temperature (> 250˚C) under non-isothermal conditions [76,77], while values ranging from 20 to 200 kJ·mol^{-1} have been reported for the isothermal carbonation of CaO above 400˚C [78–82]. The fact that we found comparable activation energies for the room temperature (14-30˚C) carbonation of the $Ca(OH)_2$ nanoparticles' films, is explained considering that in our case the process takes place at high RH (75%), rather than in dry conditions. Vance et al. had previously reported an activation energy of 7.5 kJ·mol^{-1}for the carbonation of portlandite particles around room temperature, using liquid and supercritical CO_2 [83].

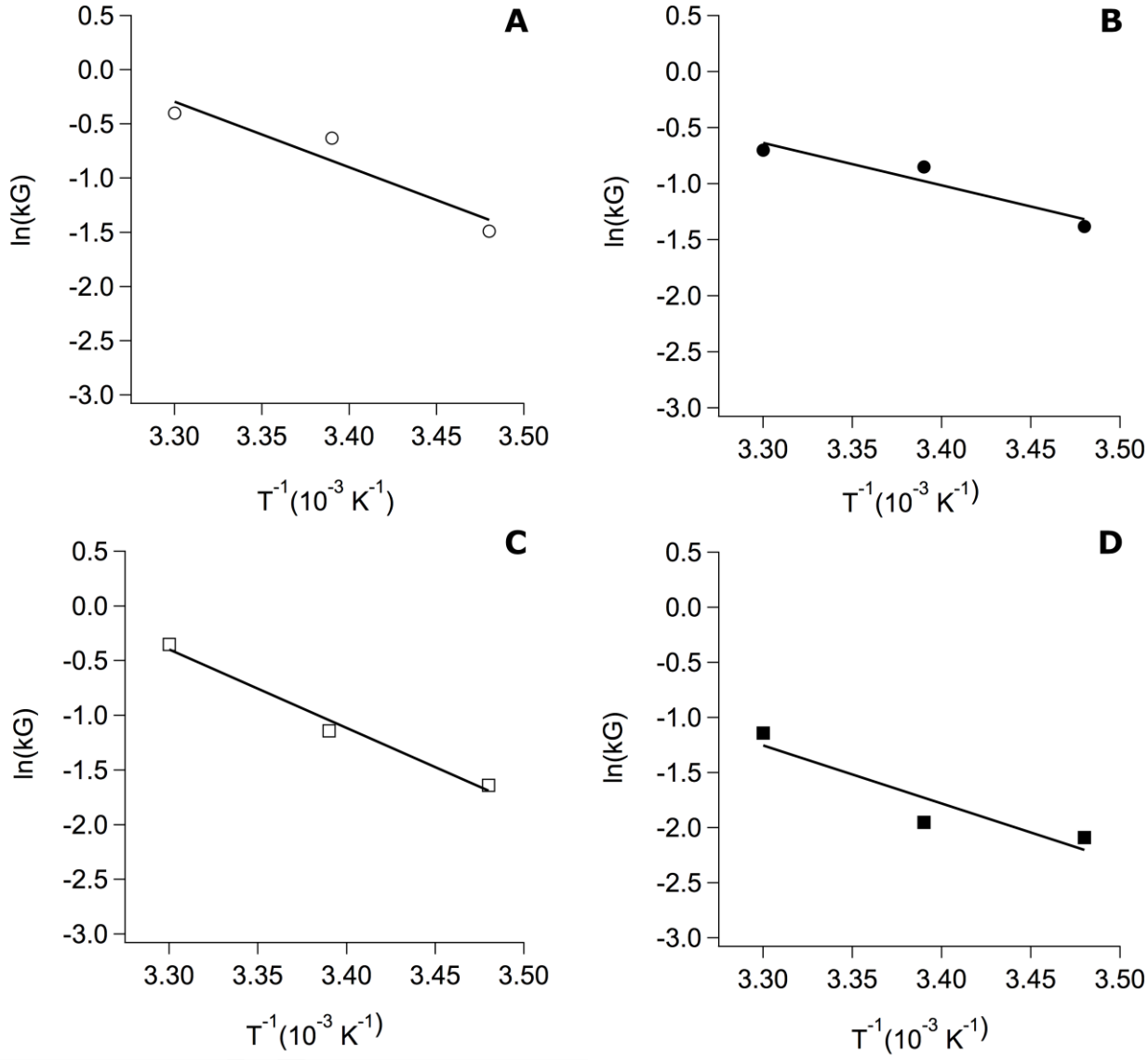

Figure 4 – Arrhenius plot (lnk_G versus 1/T) of the four systems: (A) CE system, (B) LE system, (C) CIP system, (D) LIP system.

Carbonate Polymorphs

As a side topic to the actual kinetic study, we evaluated semi-quantitatively the formation of the $CaCO_3$ phases from the carbonation of the $Ca(OH)_2$ nanoparticles. While previous studies by Rodriguez-Navarro et al. and Cizer et al.[47,52,84] have detailed the morphology and structure of the $CaCO_3$ polymorphs formed by carbonation, our aim in this contribution was to verify if the size and surface area of the $Ca(OH)_2$ nanoparticles affect the speed of formation of vaterite and calcite. FTIR was employed to evaluate the presence of $CaCO_3$ phases, as this technique, differently from X-Rays, enables monitoring both amorphous and crystalline phases over time. FTIR was previously reported in the literature to quantitatively analyze calcium carbonate polymorphs [63].
Here, the time-evolution of the following absorption bands was monitored: calcite in-plane bending (v_4) at 713 cm^{-1}, vaterite in-plane bending (v_4) at 745 cm^{-1}, and aragonite out-of-plane bending (v_2) at 854 cm^{-1} [62,63]. Besides, we monitored the presence of the broad band of ACC centered at 865 cm^{-1} (out-of-plane bending, v_2), and its evolution and shift into a narrower band centered at 876 cm^{-1} (vaterite and calcite out-of-plane bending, v_2) [62].

According to the literature, the carbonation of $Ca(OH)_2$ nanoparticles in humid air at room temperature involves the initial formation of ACC and its transformation into metastable vaterite (and minor amounts of aragonite), via a dissolution–precipitation process, followed by crystal growth [52,53,85–87]. As reported by Rodriguez-Navarro et al., building units of vaterite presumably form via heterogeneous nucleation onto ACC, and then aggregate by mesoscale assembly into nearly iso-oriented structures resembling mesocrystals. Aragonite spindle-like structures likely form after heterogeneous nucleation onto ACC; then aragonite dissolves and transforms either into calcite or into large prisms (by Ostwald ripening), and its presence is overall scarce. The stable phase, calcite, can directly nucleate and grow after dissolution of ACC/vaterite/aragonite, or nucleate on vaterite/aragonite and grow via non-classical particle-mediated aggregation or a classical ion-mediated mechanism [52].

While ethanol seems to have no significant effect on ACC formation [52], the presence of organic molecules (e.g. alcohols, alkoxides) on the surface of the $Ca(OH)_2$ particles (or grains) is known to favor the formation and kinetic stabilization of vaterite, delaying its transformation into calcite [68,84,88–90]. In few cases, the spectra of the CE, LE, CIP, and LIP systems recorded within the first hour of the carbonation process, exhibited very weak bands at 2960-2830 cm^{-1} (CH stretching), 1075 and 1050 cm^{-1} (C-O stretching), ascribable both to residual alcohol (from the drying step) or to alkoxide [91]. The latter can be due to untransformed reaction products in the case of nanoparticles obtained by solvothermal reaction, or can be formed by reaction of $Ca(OH)_2$ with short-chain alcohols during storage of the dispersions [68]. In any case, alkoxide is readily transformed into calcium hydroxide by hydrolysis in humid air.

The aforementioned polymorph evolution (ACC → vaterite → calcite) was observed for all the systems at all temperatures (14˚C, 22˚C, 30˚C), in agreement with the trend reported in the literature [52,53,85–87]. Figure 5 shows a representative example (system CE at 14˚C) where the broad band centered at 865 cm^{-1} (ACC out-of-plane bending, v_2) becomes narrower and shifts over time to 876 cm^{-1} (vaterite and calcite out-of-plane bending, v_2).

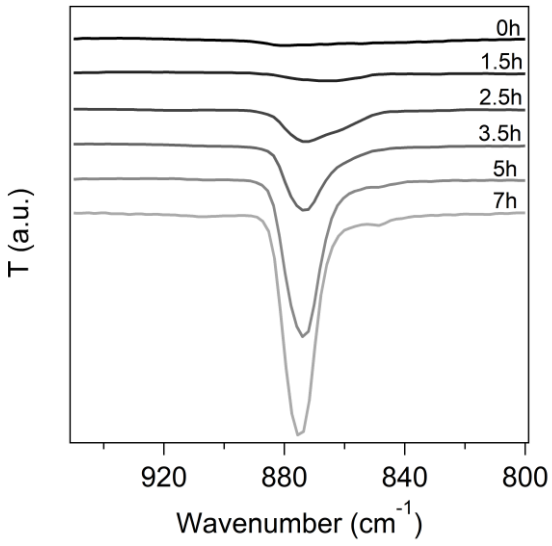

Figure 5 – Time-evolution of the carbonate out-of-plane bending absorption peak (v_2) for the CE system at 14°C: the broad band centered at 865 cm^{-1} (ACC out-of-plane bending, v_2) becomes narrower and shifts to 876 cm^{-1} (vaterite and calcite out-of-plane bending, v_2).

When temperature increases from 14 to 30˚C, the presence of ACC is observable up to progressively shorter times, i.e. up to 2h from the beginning of the $Ca(OH)_2$ transformation at 14°C, and 0.5-2h at 22°C. At 30°C, ACC is detected in the LIP system in the first 20 minutes, while it is not detected in CE, LE and CIP, as it evolves quickly into crystalline phases.

Both the vaterite band at 745 cm^{-1} and the calcite band at 713 cm^{-1} appear only after disappearance of ACC, and both phases are detected at earlier times when temperature increases. Calcite appeared after vaterite only in three cases (LE system at 14˚C and 22˚C, LIP system at 14˚C). Consistently with the literature [52,92,93], traces of aragonite were detected in the four systems, always coexisting with vaterite.

At later stages, calcite prevails on vaterite, and vaterite disappears at earlier times when temperature increases. Calcite is the sole or dominant polymorph in CE, LE and CIP after 14h at 14˚C, 7h at 22˚C, and 4h at 30˚C. Figure 6 qualitatively shows the trends of the CE system at the three temperature values. For the LIP system, at 14˚C vaterite is present after 14h together with calcite. Calcite becomes the dominant phase after 14h at 22˚C, and after 7h at 30˚C. Figures S8-S10 show the complete set of FTIR spectra for the four systems. It is worth noting that the slower time evolution of $CaCO_3$ polymorphs in LIP is consistent with the slower $Ca(OH)_2$ transformation kinetics of this system as opposed to CE, LE, and CIP.

In order to evaluate semi-quantitatively the aforementioned trends for the formation of the crystalline polymorphs, we measured the absorbance of the vaterite peak at 745 cm^{-1} (Abs^{745}), and of the calcite peak at 713 cm^{-1} (Abs^{713}). The concentration of each polymorph (c_{VAT} and c_{CALC}) was then calculated using the following formula [63]:

$$c_{VAT} = (Abs^{745}/\alpha_{VAT}^{745})$$

$$c_{CALC} = (Abs^{713}/\alpha_{CALC}^{713})$$

where α_{VAT}^{745} and α_{CALC}^{713} are respectively the values of the absorption coefficients of vaterite and calcite, which were calculated by Vagenas et al. (α_{VAT}^{745} = 21.8 mm^2 mg^{-1}; α_{CALC}^{713} = 63.4 mm^2 mg^{-1}) [63]. The concentrations were then weighted by the initial amount of available calcium hydroxide for each considered sample (i.e. KBr pellet). The weighted concentration was labeled C*. Figure 7 shows the evolution of vaterite and calcite for the CE system at all the considered temperatures. Such trends are representative of all the systems (see Figure S11-S13), even though the LIP system has a slower time evolution of the two phases, as mentioned above. The obtained results confirmed that in most cases calcite coexists with vaterite starting from the first stages of the formation of crystalline phases. Indeed, it has been shown that the formation of calcite takes place in solution through either direct (nucleation from solution) or indirect pathways (nucleation on vaterite and aragonite) [52].

Overall, the semi-quantitative evaluation showed that the polymorph evolution is slower for larger nanoparticles (with lower surface area), similarly to what observed for the conversion of $Ca(OH)_2$ into $CaCO_3$.

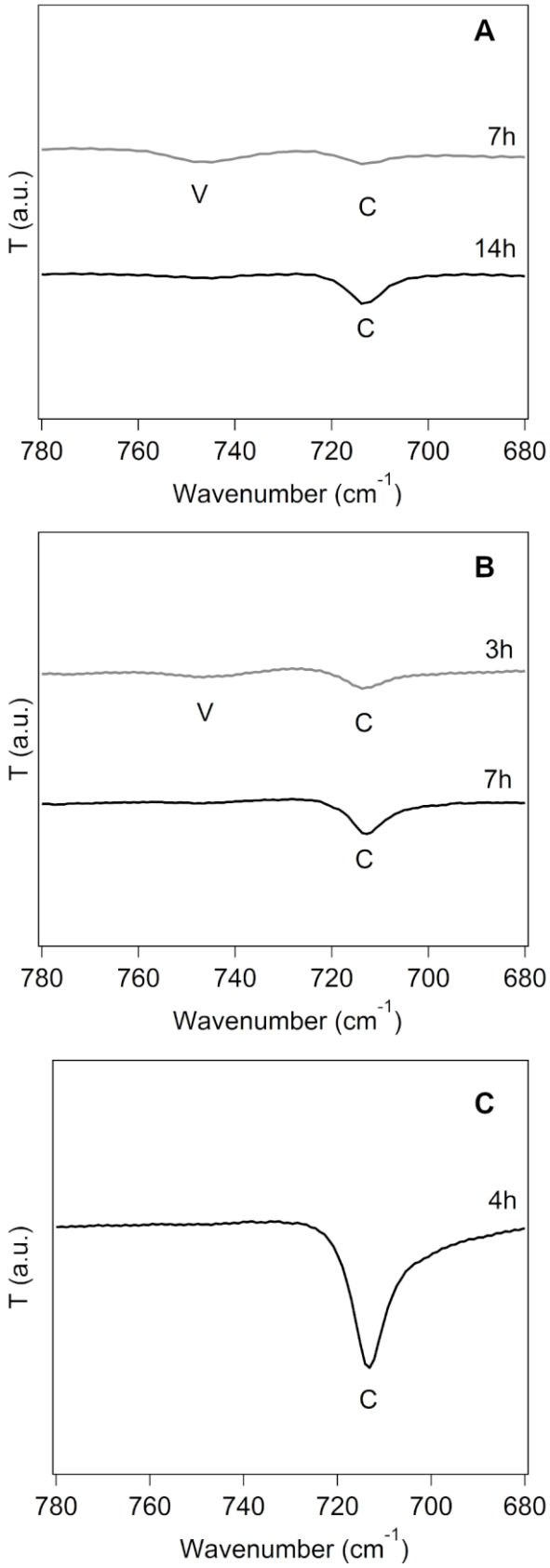

Figure 6 – FTIR spectra, showing the 780-680 cm^{-1} region, of the CE system at 14 (A), 22 (B) and 30°C (C), at different times through the carbonation process. The evolution of the in-plane bending absorption (v_4) of calcite ("C", 713 cm^{-1}) and vaterite ("V", 745 cm^{-1}) is highlighted

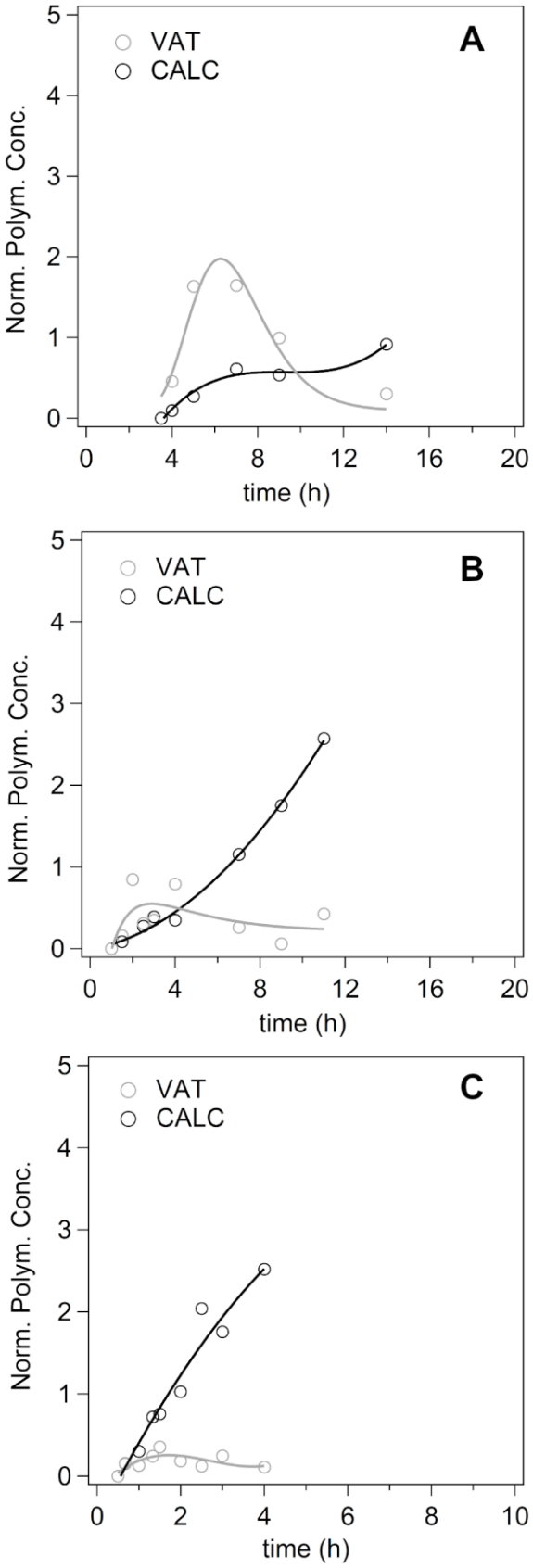

Figure 7 – Time-evolution of the vaterite and calcite weighted concentrations for the CE system at 14°C (A), 22°C (B), and 30°C (C). The solid lines are simply guides to visualize the trend of the experimental data

Conclusions

The carbonation kinetics of four different $Ca(OH)_2$ nanoparticles dispersions in humid air was investigated using for the first time the Boundary Nucleation and Growth Model (BNGM). The choice of the BNGM over Avrami-type or deceleratory models previously reported in the literature [16,50,51,54,55] was due to the necessity of taking into account systematically the separate contribution of the nucleation and of the growth of calcium carbonate phases, and also to inspect the role of the surface area of the particles in the transformation of $Ca(OH)_2$ into $CaCO_3$.

We found that in several cases fitting the time evolution of the $Ca(OH)_2$ carbonation degree (obtained by FTIR) to the generalized BNGM was possible only using narrow constraints on the value of k_B (related to the nucleation process). In any case, for all the systems at all the considered temperatures, the value of k_B is larger than that of k_G (the growth rate, at which the carbonation products fill the porosities). Moreover, in all cases the ratio between the nucleation rate per unit area of untransformed boundary, I_B, and the linear growth rate, G, is very large. Such conditions indicate that the boundary regions are densely populated with nuclei and transform early in the process with subsequent thickening of slab-like regions centered on the original boundaries. A BNGM limiting case equation was thus used to fit the process kinetics, where the transformation rate depends only on the growth process, and decreases exponentially with time; the limiting case equation provides good fitting of the experimental data, with no need of constraints.

Nanoparticles with larger dimensions and lower surface area exhibit lower k_G and transform completely at later times. This can be ascribed to the lower amount of boundaries available for the nucleation of $CaCO_3$. Nanoparticles prepared via alkoxide routes show similar k_G values, consistently with the similar particles' dimensions and surface area of these systems.

Differences in the linear growth rate of the transformed products at 22˚C were ascribed to the effect of the solvent: 2-propanol favors the aggregation of particles in the dispersions and during the formation of films; aggregation might have a different effect on the surface area of the dry $Ca(OH)_2$ films than on k_G, i.e. the two factors that determine G.

Arrhenius plots showed that the LE system exhibits the lowest activation energy, i.e. the lowest dependence of the growth rate on temperature.

The $CaCO_3$ polymorph evolution in all systems follows the trend ACC → vaterite → calcite. The prolonged presence of vaterite was explained considering that alcohol molecules, adsorbed on the surface of $Ca(OH)_2$ particles, retard the dissolution of vaterite and subsequent precipitation of calcite. Both phases are detected at earlier times when temperature increases. Later in the polymorph evolution, calcite prevails on vaterite, and vaterite disappears at earlier times when temperature increases. The polymorph evolution is slower for larger nanoparticles (with lower surface area) as observed for the conversion of $Ca(OH)_2$ into $CaCO_3$.

In conclusion, the results obtained using the BNGM corroborate and integrate those provided by deceleratory models previously proposed in the literature, but the approach proposed here led to new and detailed insight on the carbonation kinetics, where general consensus has not yet been reached. Importantly, values for the growth constant rate, overlooked by previous works [50,51,54,55], were provided in this contribution for the first time.

Future perspectives involve deepening the effects of the systems' carbonation kinetics on their behavior as consolidants, e.g. when they are applied for the strengthening of carbonate-based artistic or architectural heritage (mortars, murals, limestone, etc.); for instance, slower conversion of vaterite to calcite is expected to lead to the formation of lager crystalline domains, resulting in more cohesive $CaCO_3$ layers than the other systems. This would allow selecting the optimal system and climatic conditions for different art conservation cases, where either faster carbonation times or more cohesive carbonate crystalline networks could be desired. For instance, fast carbonation rates are desirable when the $Ca(OH)_2$ nanoparticles are used to neutralize acids on cellulose-based artifacts [3–8], while highly cohesive crystalline carbonate layers are necessary to strengthen painted surfaces in wall paintings and stone [12,24,25].

Acknowledgements

CSGI (Italian Centre for Colloid and Surface Science) and (NANORESTART project, Horizon 2020 research and innovation program under grant agreement No 646063) are gratefully acknowledged for financial support.

Bibliography

[1] M.A. Oualha, N. Amdouni, F. Laoutid, Synergistic flame-retardant effect between calcium hydroxide and zinc borate in ethylene-vinyl acetate copolymer (EVA), Polym. Degrad. Stab. 144 (2017) 315–324.

[2] P. Louwakul, A. Saelo, S. Khemaleelakul, Efficacy of calcium oxide and calcium hydroxide nanoparticles on the elimination of Enterococcus faecalis in human root dentin, Clin. Oral Investig. (2017).

[3] R. Giorgi, L. Dei, M. Ceccato, C. Schettino, P. Baglioni, Nanotechnologies for Conservation of Cultural Heritage: Paper and Canvas Deacidification, Langmuir. 18 (2002) 8198–8203.

[4] R. Giorgi, D. Chelazzi, P. Baglioni, Nanoparticles of Calcium Hydroxide for Wood Conservation. The Deacidification of the Vasa Warship, Langmuir. 21 (2005) 10743–10748.

[5] G. Poggi, R. Giorgi, N. Toccafondi, V. Katzur, P. Baglioni, Hydroxide Nanoparticles for Deacidification and Concomitant Inhibition of Iron-Gall Ink Corrosion of Paper, Langmuir. 26 (2010) 19084–19090.

[6] G. Poggi, P. Baglioni, R. Giorgi, Alkaline Earth Hydroxide Nanoparticles for the Inhibition of Metal Gall Ink Corrosion, Restaurator. 32 (2011) 247–273.

[7] G. Poggi, R. Giorgi, A. Mirabile, H. Xing, P. Baglioni, A stabilizer-free non-polar dispersion for the deacidification of contemporary art on paper, J. Cult. Herit. 26 (2017) 44–52.

[8] S. Bastone, D.F. Chillura Martino, V. Renda, M.L. Saladino, G. Poggi, E. Caponetti, Alcoholic nanolime dispersion obtained by the insolubilisation-precipitation method and its application for the deacidification of ancient paper, Colloids Surfaces A Physicochem. Eng. Asp. 513 (2017) 241–249.

[9] T. Yang, B. Keller, E. Magyari, K. Hametner, D. Günther, Direct observation of the carbonation process on the surface of calcium hydroxide crystals in hardened cement paste using an atomic force microscope, J. Mater. Sci. 38 (2003) 1909–1916.

[10] V. Daniele, G. Taglieri, A. Gregori, Synthesis of Ca(OH)2 Nanoparticles Aqueous Suspensions and Interaction with Silica Fume, Adv. Mater. Res. 629 (2013) 482–487.

[11] G. Ziegenbalg, Patent DE:10327514 B3, 2005.

[12] M. Ambrosi, L. Dei, R. Giorgi, C. Neto, P. Baglioni, Colloidal particles of Ca(OH)2: Properties and applications to restoration of frescoes, Langmuir. 17 (2001) 4251–4255.

[13] R. Giorgi, M. Ambrosi, N. Toccafondi, P. Baglioni, Nanoparticles for Cultural Heritage Conservation: Calcium and Barium Hydroxide Nanoparticles for Wall Painting Consolidation, Chem. - A Eur. J. 16 (2010) 9374–9382.

[14] C. Rodriguez-Navarro, A. Suzuki, E. Ruiz-Agudo, Alcohol dispersions of calcium hydroxide nanoparticles for stone conservation, Langmuir. 29 (2013) 11457–11470.

[15] P. D'Armada, E. Hirst, Nano-lime for consolidation of plaster and stone, J. Archit. Conserv. 1 (2012) 63–80.

[16] P. Baglioni, D. Chelazzi, R. Giorgi, E. Carretti, Y. Jaidar, N. Toccafondi, Commercial Ca(OH)2 nanoparticles for the consolidation of immovable works of art, Appl Phys A. 114 (2014) 723–732.

[17] P. López-Arce, A. Zornoza-Indart, L.S. Gomez-Villalba, R. Fort, Short- and Longer-Term

Consolidation Effects of Portlandite (CaOH)2 Nanoparticles in Carbonate Stones, J. Mater. Civ. Eng. 25 (2013) 1655–1665.
[18] I. Natali, M.L. Saladino, F. Andriulo, D. Chillura Martino, E. Caponetti, E. Carretti, et al., Consolidation and protection by nanolime: Recent advances for the conservation of the graffiti, Carceri dello Steri Palermo and of the 18th century lunettes, SS. Giuda e Simone Cloister, Corniola (Empoli), J. Cult. Herit. 15 (2014) 151–158.
[19] J. Blamey, D.Y. Lu, P.S. Fennell, E.J. Anthony, Reactivation of CaO-based sorbents for CO2capture: Mechanism for the carbonation of Ca(OH)2, Ind. Eng. Chem. Res. (2011).
[20] L. Zhao, L. Sang, C. Jun, J. Ji, H.H. Teng, Aqueous carbonation of natural brucite: Relevance to CO2 sequestration, Environ. Sci. Technol. (2010).
[21] S.E. Sawell, A.J. Chandler, T.T. Eighmy, J. Hartlén, O. Hjelmar, D. Kosson, et al., The international ash working group: A treatise on residues from MSW incinerators, Stud. Environ. Sci. 60 (1994) 3–6.
[22] C.L. Corkhill, J.W. Bridge, X.C. Chen, P. Hillel, S.F. Thornton, M.E. Romero-Gonzalez, et al., Real-time gamma imaging of technetium transport through natural and engineered porous materials for radioactive waste disposal, Environ. Sci. Technol. (2013).
[23] R.C. Ewing, Long-term storage of spent nuclear fuel, Nat. Mater. 14 (2015) 252–257.
[24] R. Giorgi, L. Dei, P. Baglioni, A New Method for Consolidating Wall Paintings Based on Dispersions of Lime in Alcohol, Stud. Conserv. 45 (2000) 154–161.
[25] P. Baglioni, E. Carretti, D. Chelazzi, Nanomaterials in art conservation, Nat. Nanotechnol. 10 (2015) 287–290.
[26] P. Baglioni, D. Chelazzi, R. Giorgi, G. Poggi, Colloid and Materials Science for the Conservation of Cultural Heritage: Cleaning, Consolidation, and Deacidification, Langmuir. 29 (2013) 5110–5122.
[27] D. Chelazzi, G. Poggi, Y. Jaidar, N. Toccafondi, R. Giorgi, P. Baglioni, Hydroxide nanoparticles for cultural heritage: Consolidation and protection of wall paintings and carbonate materials, J. Colloid Interface Sci. 392 (2013) 42–49.
[28] E. Carretti, L. Dei, Physicochemical characterization of acrylic polymeric resins coating porous materials of artistic interest, Prog. Org. Coatings. 49 (2004) 282–289.
[29] R. Giorgi, M. Baglioni, D. Berti, P. Baglioni, New Methodologies for the Conservation of Cultural Heritage: Micellar Solutions, Microemulsions, and Hydroxide Nanoparticles, Acc. Chem. Res. 43 (2010) 695–704.
[30] S. Grassi, E. Carretti, P. Pecorelli, F. Iacopini, P. Baglioni, L. Dei, The conservation of the Vecchietta's wall paintings in the Old Sacristy of Santa Maria della Scala in Siena: The use of nanotechnological cleaning agents, J. Cult. Herit. 8 (2007) 119–125.
[31] Chiantore O., Lazzari M., Photo-oxidative stability of paraloid acrylic protective polymers, Polymer (Guildf). 42 (2001) 17–27.
[32] M. Baglioni, C. Montis, D. Chelazzi, R. Giorgi, D. Berti, P. Baglioni, Polymer Film Dewetting by Water/Surfactant/Good-Solvent Mixtures: A Mechanistic Insight and Its Implications for the Conservation of Cultural Heritage, Angew. Chemie Int. Ed. 57 (2018) 7355–7359.
[33] D. Chelazzi, R. Giorgi, P. Baglioni, Microemulsions, Micelles, and Functional Gels: How Colloids and Soft Matter Preserve Works of Art, Angew. Chemie Int. Ed. 57 (2018) 7296–7303.
[34] M. Raudino, G. Selvolini, C. Montis, M. Baglioni, M. Bonini, D. Berti, et al., Polymer Films Removed from Solid Surfaces by Nanostructured Fluids: Microscopic Mechanism and Implications for the Conservation of Cultural Heritage, ACS Appl. Mater. Interfaces. 7 (2015) 6244–6253.
[35] P. Baglioni, D. Berti, M. Bonini, E. Carretti, L. Dei, E. Fratini, et al., Micelle , microemulsions , and gels for the conservation of cultural heritage, Adv. Colloid Interface Sci. 205 (2014) 361–371.

[36] E. Stefanis, C. Panayiotou, Protection of lignocellulosic and cellulosic paper by deacidification with dispersions of micro- and nano-particles of Ca(OH)2 and Mg(OH)2 in alcohols, Restaurator. 28 (2007) 185–200.
[37] V. Daniele, G. Taglieri, R. Quaresima, The nanolimes in Cultural Heritage conservation: Characterisation and analysis of the carbonatation process, J. Cult. Herit. 9 (2008) 294–301.
[38] V. Daniele, G. Taglieri, Nanolime suspensions applied on natural lithotypes: The influence of concentration and residual water content on carbonatation process and on treatment effectiveness, J. Cult. Herit. 11 (2010) 102–106.
[39] M.A.B. Sotillo, C. Rodriguez-Navarro, E. Ruiz-Agudo, K. Elert., Patent US9034100 (priority date 04.05.2010), 2015.
[40] C. Rodriguez-Navarro, E. Ruiz-Agudo, Nanolimes: From synthesis to application, Pure Appl. Chem. 90 (2018) 523–550.
[41] K. Yura, K.C. Fredrikson, E. Matijević, Preparation and properties of uniform colloidal indium compounds of different morphologies, Colloids and Surfaces. 50 (1990) 281–293.
[42] L.A. Pérez-Maqueda, L. Wang, E. Matijević, Nanosize Indium Hydroxide by Peptization of Colloidal Precipitates, Langmuir. 14 (1998) 4397–4401.
[43] B. Salvadori, L. Dei, Synthesis of Ca(OH)2 nanoparticles from diols, Langmuir. 17 (2001) 2371–2374.
[44] A. Nanni, L. Dei, Ca(OH)2 Nanoparticles from W/O Microemulsions, Langmuir. 19 (2003) 933–938.
[45] J. Xu, Q.H. Chen, Q.R. Qian, Application of hydrosoluble polymers to preparation of nanoscale calcium hydroxide, Chem. Res. Chinese Univ. 20 (2004) 229–231.
[46] S. Sequeira, C. Casanova, E. Cabrita, Deacidification of paper using dispersions of Ca(OH)2 nanoparticles in isopropanol. Study of efficiency, J. Cult. Herit. 7 (2006) 264–272.
[47] C. Rodriguez-Navarro, K. Kudłacz, Ö. Cizer, E. Ruiz-Agudo, Formation of amorphous calcium carbonate and its transformation into mesostructured calcite, CrystEngComm. 17 (2015) 58–72.
[48] H. Yagi, A. Iwazawa, R. Sonobe, T. Matsubara, H. Hikita, Crystallization of calcium carbonate accompanying chemical absorption, Ind. Eng. Chem. Fundamen. 23 (1984) 153–158.
[49] J. García-Carmona, J.G. Morales, R.R. Clemente, Morphological control of precipitated calcite obtained by adjusting the electrical conductivity in the Ca(OH)2-H2O-CO2system, J. Cryst. Growth. 249 (2003) 561–571.
[50] G. Montes-Hernandez, F. Renard, N. Geoffroy, L. Charlet, J. Pironon, Calcite precipitation from CO2-H2O-Ca(OH)2 slurry under high pressure of CO2, J. Cryst. Growth. 308 (2007) 228–236.
[51] G. Montes-Hernandez, A. Pommerol, F. Renard, P. Beck, E. Quirico, O. Brissaud, In situ kinetic measurements of gas-solid carbonation of Ca(OH)2 by using an infrared microscope coupled to a reaction cell, Chem. Eng. J. 161 (2010) 250–256.
[52] C. Rodriguez-Navarro, K. Elert, R. Ševčík, Amorphous and crystalline calcium carbonate phases during carbonation of nanolimes: implications in heritage conservation, CrystEngComm. 18 (2016) 6594–6607.
[53] D.T. Beruto, R. Botter, Liquid-like H2O adsorption layers to catalyze the Ca(OH)2/CO2solid-gas reaction and to form a non-protective solid product layer at 20°C, J. Eur. Ceram. Soc. 20 (2000) 497–503.
[54] R.M. Dheilly, J. Tudo, Y. Sebaibi, M. Quéneudec, Influence of storage conditions on the carbonation of powdered Ca(OH)2, Constr. Build. Mater. 16 (2002) 155–161.
[55] S.-M. Shih, C.-S. Ho, Y.-S. Song, J.-P. Lin, Kinetics of the Reaction of Ca(OH)2 with CO2 at Low Temperature, Ind. Eng. Chem. Res. 38 (1999) 1316–1322.
[56] A. Khawam, D.R. Flanagan, Solid-state kinetic models: Basics and mathematical fundamentals, J. Phys. Chem. B. 110 (2006) 17315–17328.

[57] J.W. Cahn, The kinetics of grain boundary nucleated reactions, Acta Metall. 4 (1956) 449–459.
[58] J.J. Thomas, A new approach to modeling the nucleation and growth kinetics of tricalcium silicate hydration, J. Am. Ceram. Soc. 90 (2007) 3282–3288.
[59] Ö. Cizer, C. Rodriguez-Navarro, E. Ruiz-Agudo, J. Elsen, D. Van Gemert, K. Van Balen, Phase and morphology evolution of calcium carbonate precipitated by carbonation of hydrated lime, J. Mater. Sci. 47 (2012) 6151–6165.
[60] Ö. Cizer, K. Van Balen, J. Elsen, D. Van Gemert, Real-time investigation of reaction rate and mineral phase modifications of lime carbonation, Constr. Build. Mater. 35 (2012) 741–751.
[61] G.L. Pesce, I.W. Fletcher, J. Grant, M. Molinari, S.C. Parker, R.J. Ball, Carbonation of Hydrous Materials at the Molecular Level: A Time of Flight-Secondary Ion Mass Spectrometry, Raman and Density Functional Theory Study, Cryst. Growth Des. 17 (2017) 1036−1044.
[62] L. Andersen, Flemming A. Brečević, Infrared Spectra of Amorphous and Crystalline Calcium Carbonate, Acta Chem. Scand. 45 (1991) 1018–1024.
[63] N. Vagenas, Quantitative analysis of synthetic calcium carbonate polymorphs using FT-IR spectroscopy, Talanta. 59 (2003) 831–836.
[64] G. Poggi, N. Toccafondi, L.N. Melita, J.C. Knowles, L. Bozec, R. Giorgi, et al., Calcium hydroxide nanoparticles for the conservation of cultural heritage: new formulations for the deacidification of cellulose-based artifacts, Appl. Phys. A. 114 (2014) 685–693.
[65] G. Poggi, N. Toccafondi, D. Chelazzi, P. Canton, R. Giorgi, P. Baglioni, Calcium hydroxide nanoparticles from solvothermal reaction for the deacidification of degraded waterlogged wood, J. Colloid Interface Sci. 473 (2016) 1–8.
[66] Technical Leaflet CaLoSiL®, Colloidal nano-particles of lime for stone and plaster consolidation, IBZ-Salzchemie GmbH & Co.KG (Germany) https://ibz-freiberg.de/produkte, (n.d.).
[67] P.A. Hassan, S. Rana, G. Verma, Making sense of brownian motion: colloid characterization by dynamic light scattering, Langmuir. 31 (2015) 3–12.
[68] C. Rodriguez-Navarro, I. Vettori, E. Ruiz-Agudo, Kinetics and Mechanism of Calcium Hydroxide Conversion into Calcium Alkoxides: Implications in Heritage Conservation Using Nanolimes, Langmuir. 32 (2016) 5183–5194.
[69] P. López-Arce, L.S. Gomez-Villalba, L. Pinho, M.E. Fernández-Valle, M.Á. de Buergo, R. Fort, Influence of porosity and relative humidity on consolidation of dolostone with calcium hydroxide nanoparticles: Effectiveness assessment with non-destructive techniques, Mater. Charact. 61 (2010) 168–184.
[70] L.S. Gomez-Villalba, P. López-Arce, M. Alvarez de Buergo, R. Fort, Structural stability of a colloidal solution of Ca(OH)2 nanocrystals exposed to high relative humidity conditions, Appl. Phys. A Mater. Sci. Process. 104 (2011) 1249–1254.
[71] E. Carretti, D. Chelazzi, G. Rocchigiani, P. Baglioni, G. Poggi, L. Dei, Interactions between Nanostructured Calcium Hydroxide and Acrylate Copolymers: Implications in Cultural Heritage Conservation, Langmuir. 29 (2013) 9881–9890.
[72] J.W. Christian, The theory of transformations in metals and alloys, 3rd edition, Pergamon Press, Oxford, 2002., 2002.
[73] S. Del Buffa, E. Fratini, F. Ridi, A. Faraone, P. Baglioni, State of Water in Hydrating Tricalcium Silicate Pastes: The Effect of a Cellulose Ether, J. Phys. Chem. C. 120 (2016) 7612–7620.
[74] H. Taylor, Cement Chemistry, Thomas Telford. 2nd ed. London: Thomas Telford Publishing, 1997.
[75] S. Garrault, T. Behr, A. Nonat, Formation of the C-S-H layer during early hydration of tricalcium silicate grains with different sizes, J. Phys. Chem. B. 110 (2006) 270–275.

[76] G. Montes-Hernandez, R. Chiriac, F. Toche, F. Renard, Gas-solid carbonation of Ca(OH)2and CaO particles under non-isothermal and isothermal conditions by using a thermogravimetric analyzer: Implications for CO2capture, Int. J. Greenh. Gas Control. 11 (2012) 172–180.
[77] V. Nikulshina, M.E. Gálvez, A. Steinfeld, Kinetic analysis of the carbonation reactions for the capture of CO2from air via the Ca(OH)2-CaCO3-CaO solar thermochemical cycle, Chem. Eng. J. 129 (2007) 75–83.
[78] M. Ramezani, P. Tremain, E. Doroodchi, B. Moghtaderi, Determination of Carbonation/Calcination Reaction Kinetics of a Limestone Sorbent in low CO2 Partial Pressures Using TGA Experiments, Energy Procedia. 114 (2017) 259–270.
[79] S.K. Bhatia, D.D. Perlmutter, Effect of the product layer on the kinetics of the CO2-lime reaction, AIChE J. 29 (1983) 79–86.
[80] H. Gupta, L.S. Fan, Carbonation-calcination cycle using high reactivity calcium oxide for carbon dioxide separation from flue gas, Ind. Eng. Chem. Res. 41 (2002) 4035–4042.
[81] P. Sun, J.R. Grace, C.J. Lim, E.J. Anthony, Determination of intrinsic rate constants of the CaO-CO2reaction, Chem. Eng. Sci. 63 (2008) 47–56.
[82] G. Grasa, I. Martínez, M.E. Diego, J.C. Abanades, Determination of CaO carbonation kinetics under recarbonation conditions, Energy and Fuels. 28 (2014) 4033–4042.
[83] K. Vance, G. Falzone, I. Pignatelli, M. Bauchy, M. Balonis, G. Sant, Direct Carbonation of Ca(OH)<inf>2</inf> Using Liquid and Supercritical CO<inf>2</inf>: Implications for Carbon-Neutral Cementation, Ind. Eng. Chem. Res. 54 (2015) 8908−8918.
[84] F. Manoli, E. Dalas, Spontaneous precipitation of calcium carbonate in the presence of ethanol, isopropanol and diethylene glycol, J. Cryst. Growth. 218 (2000) 359−364.
[85] M.H. Nielsen, S. Aloni, J.J. De Yoreo, In situ TEM imaging of CaCO3 nucleation reveals coexistence of direct and indirect pathways, Science (80-.). 345 (2014) 1158–1162.
[86] J.J. De Yoreo, P.U.P.A. Gilbert, N.A.J.M. Sommerdijk, R.L. Penn, S. Whitelam, D. Joester, et al., Crystallization by particle attachment in synthetic, biogenic, and geologic environments, Science (80-.). 349 (2015) aaa6760.
[87] T. Ogino, T. Suzuki, K. Sawada, The formation and transformation mechanism of calcium carbonate in water, Geochim. Cosmochim. Acta. 51 (1987) 2757–2767.
[88] L. Zhang, L.H. Yue, F. Wang, Q. Wang, Divisive effect of alcohol-water mixed solvents on growth morphology of calcium carbonate crystals, J. Phys. Chem. B. 112 (2008) 10668–10674.
[89] K.K. Sand, J.D. Rodriguez-Blanco, E. Makovicky, L.G. Benning, S.L.S. Stipp, Crystallization of CaCO3 in water-Alcohol mixtures: Spherulitic growth, polymorph stabilization, and morphology change, Cryst. Growth Des. 12 (2012) 842–853.
[90] K.S. Seo, C. Han, J.H. Wee, J.K. Park, J.W. Ahn, Synthesis of calcium carbonate in a pure ethanol and aqueous ethanol solution as the solvent, J. Cryst. Growth. 276 (2005) 680–687.
[91] X. Liu, X. Piao, Y. Wang, S. Zhu, Calcium Ethoxide as a Solid Base Catalyst for the Transesterification of Soybean Oil to Biodiesel, Energ. Fuel. 22 (2008) 1313−1317.
[92] P. López-Arce, L.S. Gómez-Villalba, S. Martínez-Ramírez, M. Álvarez de Buergo, R. Fort, Influence of relative humidity on the carbonation of calcium hydroxide nanoparticles and the formation of calcium carbonate polymorphs, Powder Technol. 205 (2011) 263–269.
[93] L. Gomez-Villalba, P. López-Arce, R. Fort, Nucleation of CaCO3 polymorphs from a colloidal alcoholic solution of Ca(OH)2 nanocrystals exposed to low humidity conditions, Appl. Phys. A Mater. Sci. Process. 106 (2012) 213–217.

Graphical abstract